The International Journal of Advanced Manufacturing Technology
https://doi.org/10.1007/s00170-023-12566-9

ORIGINAL ARTICLE

Investigation of 300M ultra-high-strength steel deposited by wire-based gas metal arc additive manufacturing

Jun Wang[1] · Chenglei Diao[1] · Mark Taylor[2] · Chong Wang[1] · Ed Pickering[2] · Jialuo Ding[1] · Misael Pimentel[3] · Stewart Williams[1]

Received: 24 September 2023 / Accepted: 21 October 2023

Abstract
300 M ultra-high-strength steel (UHSS) is widely used to produce landing gear components for aircraft. The conventional manufacturing route for these components involves extensive machining and significant material wastage. Here, the application of wire-based gas metal arc additive manufacturing to produce 300 M UHSS parts was investigated. In particular, the influence of torch shielding atmosphere on the process stability and material performance of 300 M UHSS was investigated. The shielding gases used for comparison are pure Ar, Ar with 2.5% CO_2, Ar with 8% CO_2, Ar with 20% CO_2, and Ar with 2% CO_2 and 38% He. It was found that the arc length decreased, the transfer mode changed from spray to droplet mode, and spattering became more severe as the CO_2 proportion increased. Additionally, replacing Ar with He led to a broader arc core, and a slightly shorter arc length and maintained a spray transfer, which decreased spatter. The wall surface roughness followed the trend in spatter, becoming worse with the increasing CO_2 proportion, and better with He addition. Adding CO_2 and He in pure Ar significantly increased the bead and wall width. The microstructure and mechanical properties exhibited a strong location dependence in the as-built state, with fresh martensite and higher strength in the top region, and tempered martensite and better ductility in the reheated bulk. Generally, torch shielding gas composition appeared to have no significant effect on the microstructure evolution. This study provides a reference for the subsequent application of gas metal arc additive manufacturing to aircraft landing gear mass production to achieve a high deposition rate and process stability simultaneously.

Keywords 300M ultra-high-strength steel · Wire arc additive manufacturing · Process stability · Microstructure · Mechanical properties

1 Introduction

Benefiting from high strength, high fracture toughness, and excellent fatigue resistance, 300 M ultra-high-strength steel (UHSS) has been extensively applied in the aerospace field for manufacturing aircraft landing gears [1, 2]. However, it has intrinsic shortcomings, including stress concentration sensitivity, making 300 M UHSS challenging to be processed into complex structures using conventional forging techniques [3]. Moreover, a massive post-machining workload is required after the forging process, significantly reducing the material utilisation rate and prolonging the lead time [4]. To address this, additive manufacturing (AM) offers an alternative with great promise for fabricating complex parts of 300 M owing to the superiorities of near-net-shape forming, high cost-effectiveness, and shortening of the production cycle [5, 6].

In recent years, increasing attention has been attracted to producing 300 M steel structures using AM methods, but this has mainly focused on applying laser-based AM technologies. Liu et al. [7] took the lead in researching the laser direct energy deposition of 300 M UHSS. Barr et al. [8] studied the influence of delay duration between tracks and layers in the 300 M UHSS laser cladding process to realise an in-situ quenching and tempering treatment to tailor microstructure. Jing et al. [1,

✉ Jun Wang
jun.wang.123@cranfield.ac.uk

[1] Welding and Additive Manufacturing Centre, Cranfield University, Cranfield MK43 0AL, UK

[2] Department of Materials, Henry Royce Institute Hub Building, The University of Manchester, Manchester M13 9PL, UK

[3] Advanced Forming Research Centre, University of Strathclyde, 85 Inchinnan Drive, Renfrewshire PA4 9LJ, UK

Published online: 01 November 2023

3, 9, 10] systematically investigated the microstructural evolution and mechanical properties of selective laser melted (SLM) 300 M UHSS within an optimal energy density window. The tensile strength of the SLM 300 M UHSS was revealed to be insensitive to the laser power, while the ductility was greatly affected by it. It can be seen from the above that research on laser-based AM deposited 300 M steel has progressed considerably, while the investigations regarding wire-arc additive manufacturing (WAAM) deposited counterparts are still scarce.

Compared to laser-based AM technologies, WAAM offers significant superiorities in achieving a higher deposition rate, minimising material loss, and allowing to use low-cost equipment and consumables, therefore exhibiting great potential for manufacturing large-scale near-net-shape metallic structures [11–15]. Thus, this technique keeps attracting significant attention in producing components from a variety of metallic materials [16–20]. Among the various electric arc categories suitable for WAAM, gas metal arc (GMA) possesses a high arc efficiency benefiting from its consumable electrode and a higher tolerance for path planning and omni-directivity when compared with non-consumable categories (e.g., gas tungsten arc (GTA) and plasma transfer arc (PTA)). Therefore, GMA is the first choice for part building whenever feasible. Xiong et al. [4] fabricated 300 M UHSS thin-walled structures using the cold metal transfer (CMT) (a variant of GMA)–based WAAM and further evaluated the role of interlayer temperature on the microstructure and mechanical performance. However, the deposition rate in the CMT process is comparatively low because of a low wire feed speed limit (8 m/min when the wire diameter is 1.2 mm). Therefore, in terms of industrial applications and development, significant gaps in the research area concerning GMA-WAAM 300 M UHSS components need to be filled.

It has been reported that in GMA-WAAM processes, the shielding gas significantly affects the welding quality, including bead morphology, surface condition, defect formation, spatter level, and microstructure evolution [21]. The most common shielding gases, Ar, CO_2, and O_2, are widely used in the GMA welding of steels in the form of a single gas or mixture, with varied volume proportions according to the chemical compositions of the welding materials [22]. Due to the high susceptibility of 300 M UHSS to oxidation, O_2 can be excluded as the candidate for the local shielding gas during the deposition. However, more research has yet to be conducted regarding the appropriate shielding gas composition for depositing 300 M UHSS components using GMA-WAAM.

In this investigation, the GMA-WAAM technique is applied to deposit defect-free 300 M UHSS. Meanwhile, the influences of shielding gas compositions (pure Ar, Ar-CO_2 mixture, and Ar-He-CO_2 combination) on the process stability, morphology, microstructure, and mechanical performance of 300 M UHSS deposited by GMA-WAAM are systematically analyzed.

2 Experimental

2.1 Materials and GMA-WAAM setup

300 M UHSS wire with a diameter of 1.2 mm was used as the feedstock, and S355 steel plates with 300 mm × 200 mm × 12 mm were used as the substrates. The chemical compositions of the two materials are listed in Table 1. Figure 1a schematically shows the experimental setup for the GMA-WAAM process. The entire setup was placed in an enclosure filled with pure argon gas with an oxygen level controlled below 800 ppm. An EWM power source integrated with a wire feeder was used to provide the electric arc and feed the wire. An arc monitor was connected to the power source to monitor the arc current and voltage. A CMOS camera was placed on the side of the melt pool to monitor the metal transfer and melt pool behavior. The substrate was fixed to a workbench by clamps, and the motion of the torch was controlled by a 6-axis ABB robot. To investigate the influence of torch shielding atmosphere compositions on the process, deposit morphology, microstructure, and mechanical performance of the GMA-WAAM 300 M UHSS structures, single-layer beads and multi-layer single-pass wall structures were deposited using five different commercial shielding gases, including pure Ar, 97.5% Ar + 2.5% CO_2, 92% Ar + 8% CO_2, 80% Ar + 20% CO_2, and 60% Ar + 38% He + 2% CO_2, with key process parameters listed in Table 2 and Table 3. The deposition experiments were performed in a flexible transparent enclosure purged with pure argon (oxygen content < 800 ppm). For single-pass wall deposition, the travel direction rotated 180° between each deposition pass and the interlayer temperature was monitored and controlled at just below 100 °C. A total of 16 layers were deposited for each single-pass wall structure.

Table 1 Chemical composition in wt% of 300 M UHSS and S355 substrate

Materials	C	Si	Mn	P	S	Cr	Mo	Ni	V	Cu	Fe
300 M UHSS wire	0.39–0.44	1.5–1.8	0.6–0.9	< 0.015	< 0.015	0.7–0.95	0.3–0.45	1.65–2	0.05–0.1	-	Bal
S355 steel substrate	≤ 0.20	≤ 0.55	≤ 1.60	≤ 0.025	≤ 0.025	-	-	-	-	≤ 0.55	Bal

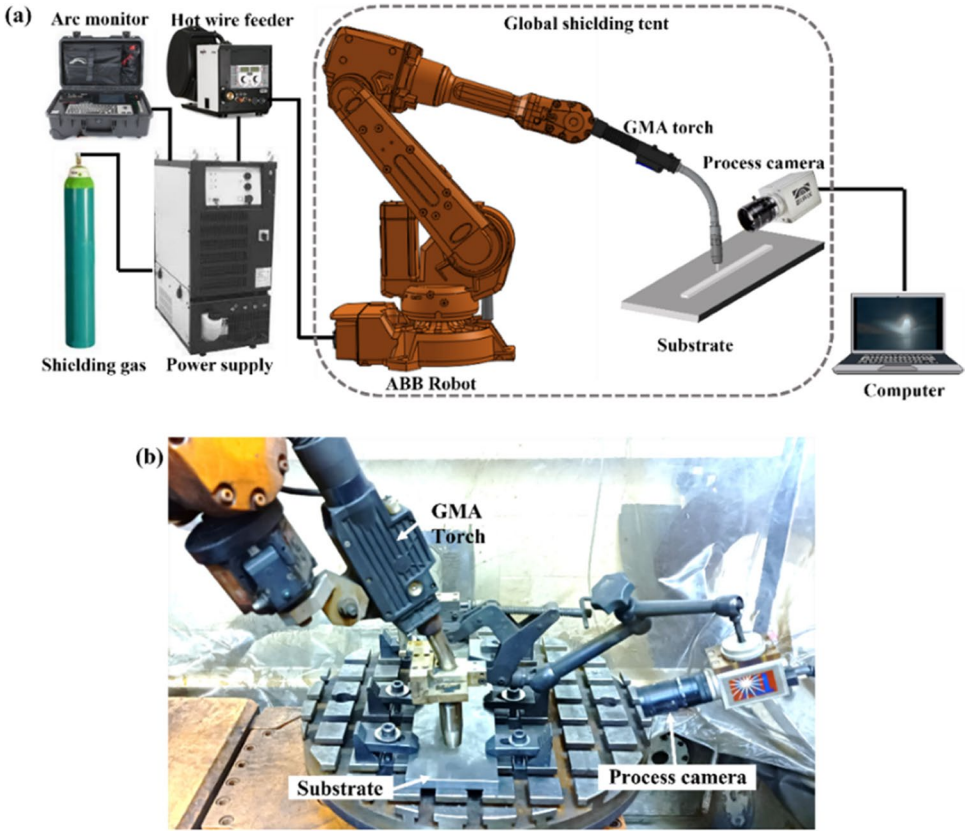

Fig. 1 Experimental setup: **a** schematic diagram for GMA-WAAM system and **b** view from inside the tent

Table 2 Deposition processing parameters used to produce the 300 M UHSS thin-walled structures

Parameters	Value
Wire feeding speed (WFS)	9.5 m/min
Torch travel speed (TS)	12 mm/s
Bead length	150 mm
Nozzle to substrate stand-off	16 mm
Shielding gas flowrate	25 L/min
Interlayer dwell time	8 min
Deposition layers	16 layers

Table 3 Deposition cases correspond to various local shielding gas compositions

Deposition cases	Local shielding gas composition (vol%)
Bead 0 (B0)	100% Ar
Bead 1 (B1); thin wall 1 (W1)	97.5% Ar + 2.5% CO_2
Bead 2 (B2); thin wall 2 (W2)	92% Ar + 8% CO_2
Bead 3 (B3); thin wall 3 (W3)	80% Ar + 20% CO_2
Bead 4 (B4); thin wall 4 (W4)	60% Ar + 38% He + 2% CO_2

2.2 Characterization

Figure 2 shows the sample extraction positions, dimensions, and reference frame. Full-height samples with a thickness of 5 mm were extracted from the normal-building (ND-BD) plane for metallographic observation. After being ground and polished, they were etched in 2% Nital (nitric acid in ethanol) to reveal the microstructure. Large-scale stitched macrographs were obtained using a microscope with an automated stage scanning function. The microstructure was then analyzed using a scanning electron microscope (SEM) equipped with energy-dispersive spectrometry (EDS) detector with an accelerating voltage of 20 kV. Small crystallographic orientation maps were obtained using a field emission gun SEM equipped with an electron backscattered diffraction (EBSD) detector with an accelerating voltage of 15 kV, a beam current of 6.5 nA, and a step size of 0.3 µm. The big-area EBSD map was obtained by a Thermo Scientific Apreo SEM with an Oxford Instrument Symmetry-2 detector, using 20-kV accelerating voltage, 51-nA beam current, and 1.2-µm step size. EBSD data was then post-processed using Oxford Instruments' AZtecCrystal software. Prior austenite grains (PAGs) were reconstructed using the Nishiyama-Wasserman orientation relationship after filling

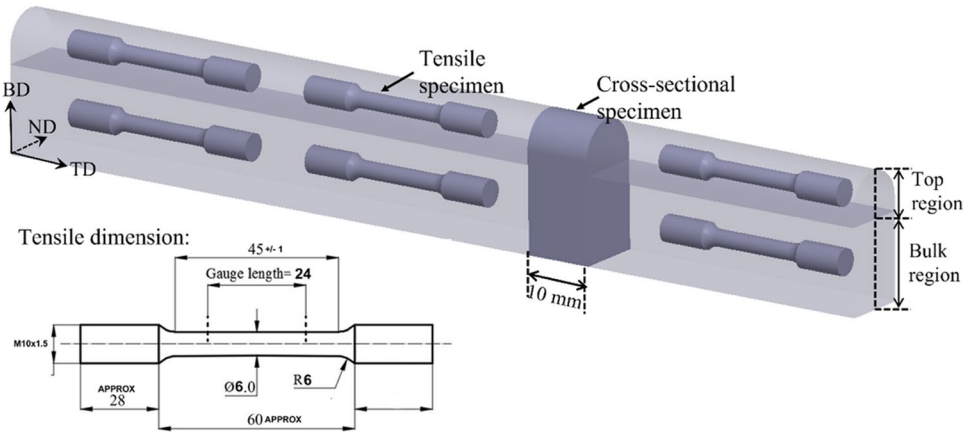

Fig. 2 Sample preparations including location and dimension. The sample reference frame includes heat source translation direction (TD), building direction (BD), and normal direction (ND)

in non-indexed pixels. The microhardness transition along the central line of the metallographic samples was examined from the bottom (the area near the substrate) to the top of the wall structure. It was measured using a hardness tester with a load of 300 g and a spacing of 1 mm. Round tensile specimens with a gauge length of 24 mm in the spirit of ASTM E8 standard were extracted from the top and bulk regions in TD to evaluate the mechanical properties on an Instron 5500R machine at room temperature with a constant strain rate of 1 mm/min. Three sets of tensile coupons were taken from each position of each wall structure to ensure data reliability. The resulting fracture surfaces were checked by SEM.

3 Results and discussion

3.1 Process stability and surface finish

Figure 3 shows the typical arc characteristics of deposition processes under different local shielding atmospheres. A pure Ar shielding gas is shown as a reference in Fig. 3a, in which undesirable arc instability occurred, which is consistent with previous research [23]. Clearly, the arc length (L) decreased with the increase of CO_2 addition in the shielding gas, as shown in Fig. 3b–d. When the CO_2 content was 2.5%, the arc length was long enough to maintain

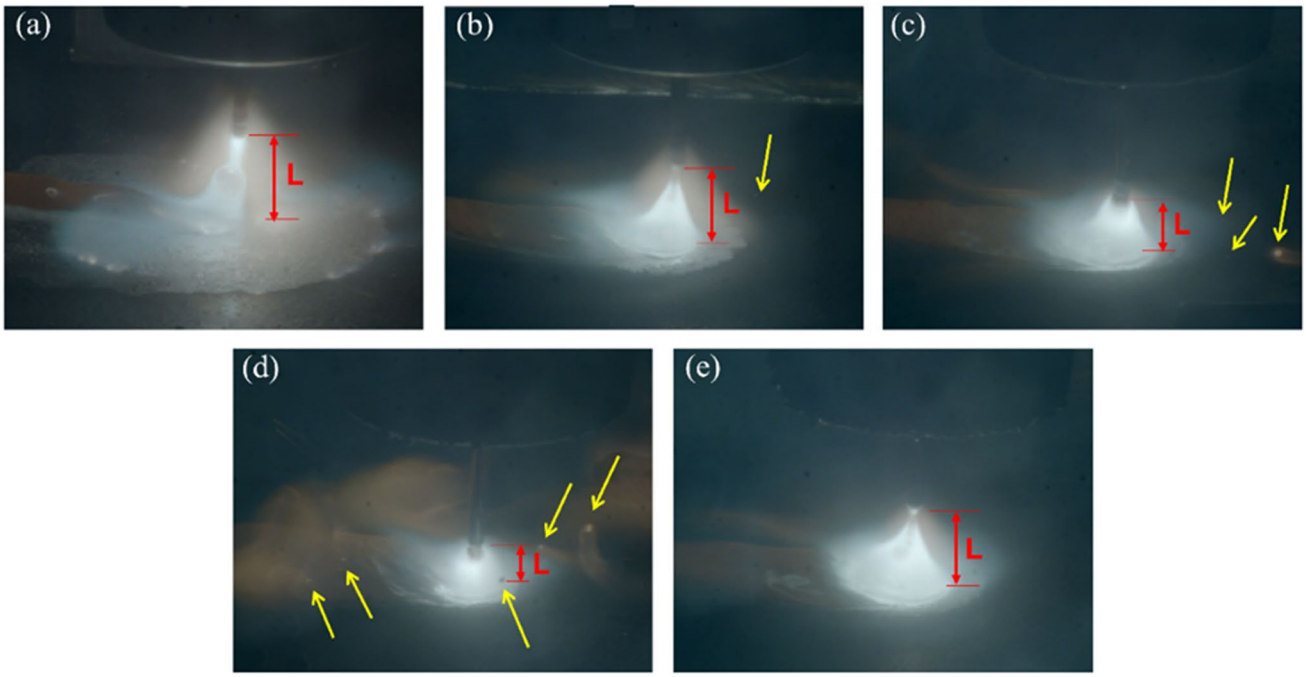

Fig. 3 Arc characteristics of deposition processes under different local shielding atmospheres: **a** pure Ar, **b** 97.5% Ar + 2.5% CO_2, **c** 92% Ar + 8% CO_2, **d** 80% Ar + 20% CO_2, and **e** 60% Ar + 38% He + 2% CO_2

a spray metal transfer mode. When the CO_2 content was increased to 8%, the arc length significantly decreased, and a globular metal transfer took place. This is because CO_2 is an electronegative gas with a higher ionization potential compared to inert gases like Ar. More CO_2 introduced into the shielding gas mixture will increase the electrical conductivity of the arc plasma, leading to a more stable arc that is easier to maintain at a shorter length [24]. In addition, alongside adding 2–2.5% of CO_2 in the shielding gas mixture, replacing 38% of Ar with He led to a broader arc core, a slightly shorter arc length and maintained a spray transfer, as shown in Fig. 3e. This is because He has a higher thermal conductivity than Ar, which increases the distance over which heat can flow.

Concurrent with the change from spray transfer to globular transfer, increasing the CO_2 portion increased spatter, as shown by the adherence of metal particles to the walls in Fig. 4. More metal particles adhered to the side surface can be found with increasing CO_2 proportion, meaning the surface roughness became coarser due to the severer spatter, leading to worse surface quality. Hence, surface finish quality was degraded with increasing CO_2 portion. A comparatively improved surface quality was found when replacing 38% of Ar with He under ~2% CO_2 (Fig. 5a, d), benefiting from a steady deposition process with less spatter generation. This can be attributed to generating a more constricted arc plasma with higher energy density resulting from the increasing CO_2 content, thereby leading to more heat transferred [24].

3.2 Macro-morphologies of the beads and walls

The bead morphologies deposited under different local shielding are displayed in Fig. 5, where bead dimensions are indicated. By comparing Fig. 5a and b, it can be seen that adding CO_2 in pure Ar increased both the bead width and height. CO_2 possesses a higher thermal conductivity than Ar, especially at the comparatively low temperatures that normally occur nearby the workpiece, so the electron work function will be reduced by the reaction between CO_2 and the melt pool, resulting in more heat being transferred to the workpiece and more material being melted [24]. In this case, more energy will be transferred to the boundary of the melt pool, and the fluid in the melt pool flows more strongly downwards, giving rise to both the increase in bead width and height [24]. The bead width and HAZ width became broader with the increase of CO_2 content from 2.5% to 20%, as shown in Fig. 5b–d. Also, replacing 38% of Ar with He led to a larger bead width and height (Fig. 5b and e). This is because He has a lower density but higher thermal conductivity than Ar, leading to more heat being transferred from the arc core to the arc periphery, which increases the arc potential gradient for energy loss compensation [24]. The bead dimensions remained similar when replacing 38% of Ar with He alongside ~2% CO_2, indicating He has less effect on heat transfer than CO_2. Following checking of the bead morphologies processed under various local shielding gas mixtures, the pure Ar build was excluded from further investigations owing to poor process stability and unsatisfying resulting morphology.

The changes in bead dimensions resulted in changes in wall height, as shown in Fig. 6. A decreasing trend in wall height can be found when CO_2 content in the shielding gas mixture increased from 2.5 to 8%, in line with the bead height results. However, with a further increase to 20%, the wall height does not decrease as expected. This is likely to be related to the misalignment deviation between the heat source and the centerline. Regarding wall width, the narrowest wall width could be found in W3 due to the material loss caused by the severest spattering phenomenon during the deposition process.

Fig. 4 Side surface morphology of single-pass 300 M wall processes under different local shielding gas mixtures: **a** 97.5% Ar + 2.5% CO_2, **b** 92% Ar + 8% CO_2, **c** 80% Ar + 20% CO_2, and **d** 60% Ar + 38% He + 2% CO_2

3.3 Wall meso-structure and microstructure

The etched cross-sections shown in Fig. 6 reveal a number of meso-scale features that need to be explained. First, there is a distinct light-etching region at the top of the build (roughly five layers high) followed by a darker-etching region that comprises the bulk of the build. Second, there is a "transition" region between the top and bulk regions of each build, where light- and dark-etching regions interpenetrate. Third, there are dark-etching bands and light-etching bands present periodically throughout the builds—the dark-etching bands, slightly inclined to the horizontal plane, only appear in the bulk material, whereas the curved light-etching bands appear throughout the bulk and top of the builds. Each of these features will be discussed in turn below.

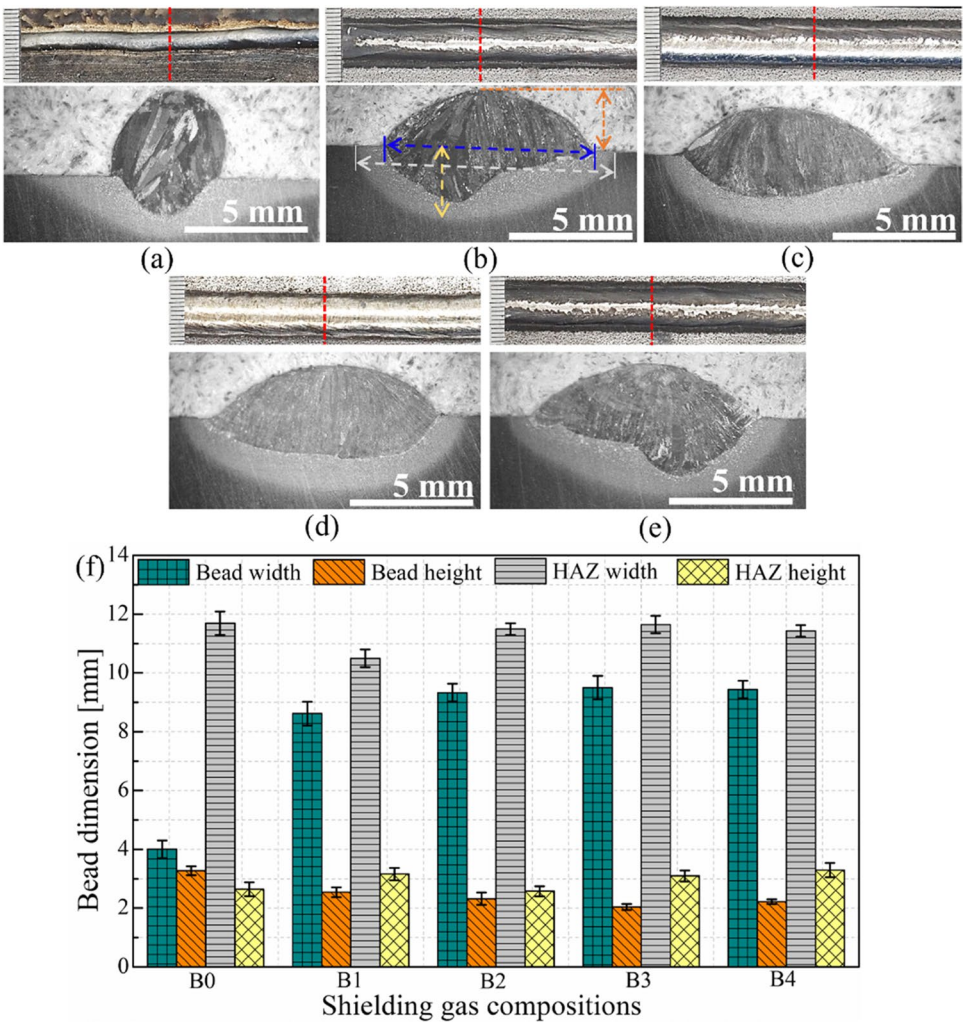

Fig. 5 Bead shapes and profiles under different local shielding gas conditions: **a** pure Ar, **b** 97.5% Ar + 2.5% CO_2, **c** 92% Ar + 8% CO_2, **d** 80% Ar + 20% CO_2, and **e** 60% Ar + 38% He + 2% CO_2; **f** bead dimension comparison

3.3.1 The top region vs the bulk

The top few layers in each build appear distinct from the bulk of the build since they were heated above the alloy's Ac_3 temperature by the last pass, transforming fully to austenite. This austenite then cooled quickly to room temperature, forming fresh martensite (here referred to as M_F), which etches lighter when viewed in an optical microscope. According to the continuous cooling transformation diagram of 300 M steel [25], the martensite transformation will take place and be predominant during cooling processes with rates above 1 °C/s, and the cooling rate during the WAAM process is normally between 10 and 100 °C/s [26]. This top region microstructure was examined using SEM, as shown in Fig. 7. Laths consistent with martensite are present, and some needle-like carbides with specific habit planes can be observed inside the martensitic lath substructures, which are likely to be products of auto-tempering of the martensite during cooling [27]. The dark-etching bulks of the builds (Fig. 8) displayed a microstructure consistent with tempered martensite, which etches more darkly (in optical images) versus as-quenched martensite. The presence of tempered martensite is to be expected as the thermal cycles experienced by the build (below the Ac_1 temperature) would not form any austenite but would temper any M_F formed previously. Through comparison, the martensitic structure (e.g., morphology and size) hardly showed any difference with varying shielding gas mixtures.

3.3.2 The transition region

A transition region, with a thickness of around 0.5 mm, was observed between the top and bulk regions in all builds, shown in Fig. 6. This possessed a distinct microstructure of irregular intertwined mixtures of light-etching and dark-etching areas in the optical micrographs. SEM images of this region are shown in Fig. 9. It is observed that the dark-etching regions in the SEM images are composed of M_F, while the light-etching regions mainly consist of tempered martensite (M_T) (note: this contrast is the reverse of that in

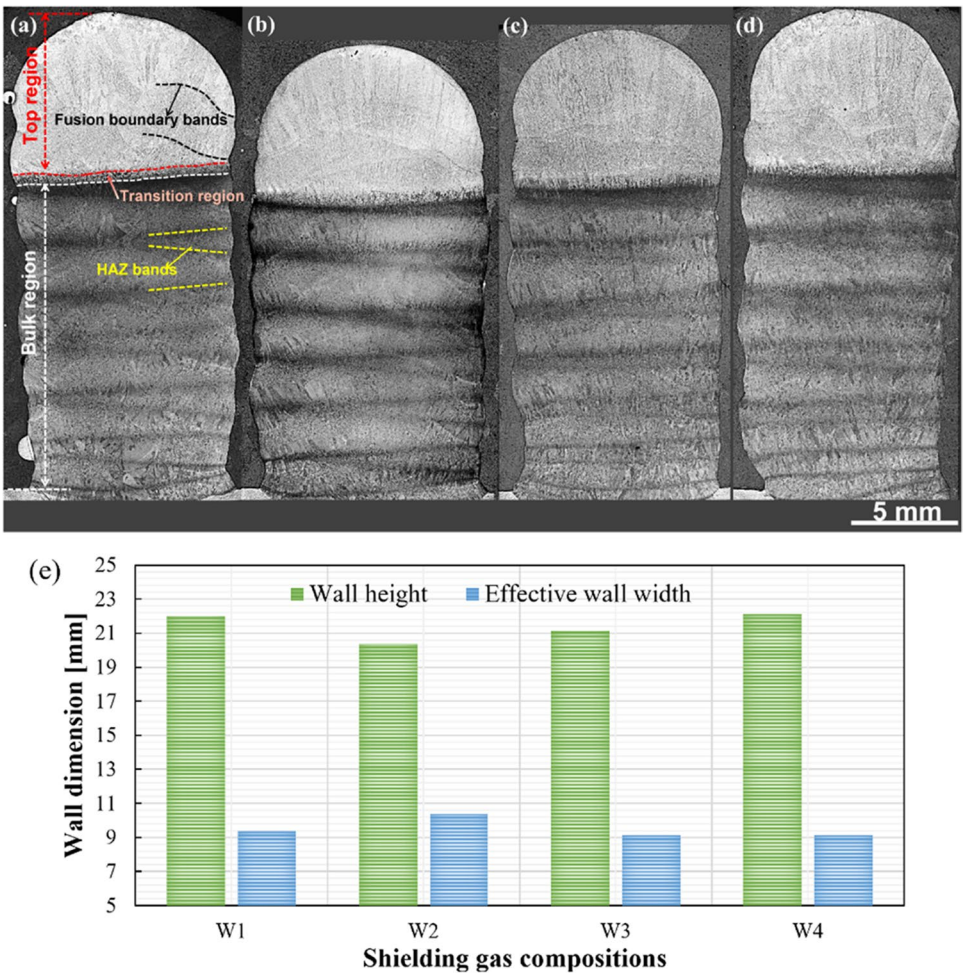

Fig. 6 Cross-sectional morphologies of the single-pass wall structures deposited under different local shielding atmospheres: **a** W1, **b** W2, **c** W3, **d** W4, and **e** the corresponding dimension data. HAZ bands and fusion boundary bands are highlighted in **a** and are also present in **b**–**d**

the optical images, Fig. 6, where M_F appears light). Hence, these transition regions are considered to experience a peak reheating temperature between Ac_1 and Ac_3 in the final pass, as in the intercritical HAZ region of a weld, where similar microstructures can be observed [28]. All the transition regions appear similar when comparing the builds with different shielding gases.

3.3.3 HAZ bands and fusion boundaries

The dark-etching bands, hereafter referred to as HAZ (heat-affected zone) bands, appear to be highly tempered regions that have experienced temperatures just below Ac_1. This is evidenced by the fact that the top HAZ band in each build appears directly below the intercritically annealed transition region. This is consistent with the conclusions drawn by Li et al. [29], who investigated HAZ bands of WAAM C-Mn steel. Once formed, these HAZ bands are not eliminated by subsequent reheating below Ac_1 and thus survive until deposition is completed. The bands would be expected to comprise a higher fraction of coarser carbides than the material between them (the inter-band bulk), owing to the higher temperatures reached in the bands (up to Ac_1). Their dark-etching appearance in optical micrographs is consistent with a higher fraction of carbides and/or the carbides being coarser.

The HAZ bands' slight inclination to the horizontal plane (rather than being perfectly horizontal) could be attributed to the slight misalignment error of the heat source relative to the wall centerline when the worktable was rotated 180° between each layer [30]. It can be seen that the HAZ bands in W2 (Fig. 6) are even more skewed against each other compared with those in other walls, indicating that the misalignment error during the W2 deposition process is comparatively larger. Additionally, the spacing of the HAZ bands in the samples is somewhat irregular (sometimes apparently overlapping). The build sequence and heat dissipation can likely explain this: if the torch passes over the same point in quick succession, then the bands are closely spaced owing to little time for heat dissipation, but if there is more time between each layer (or improved heat dissipation, as seen near the bottom of the builds), then the bands are more widely spaced.

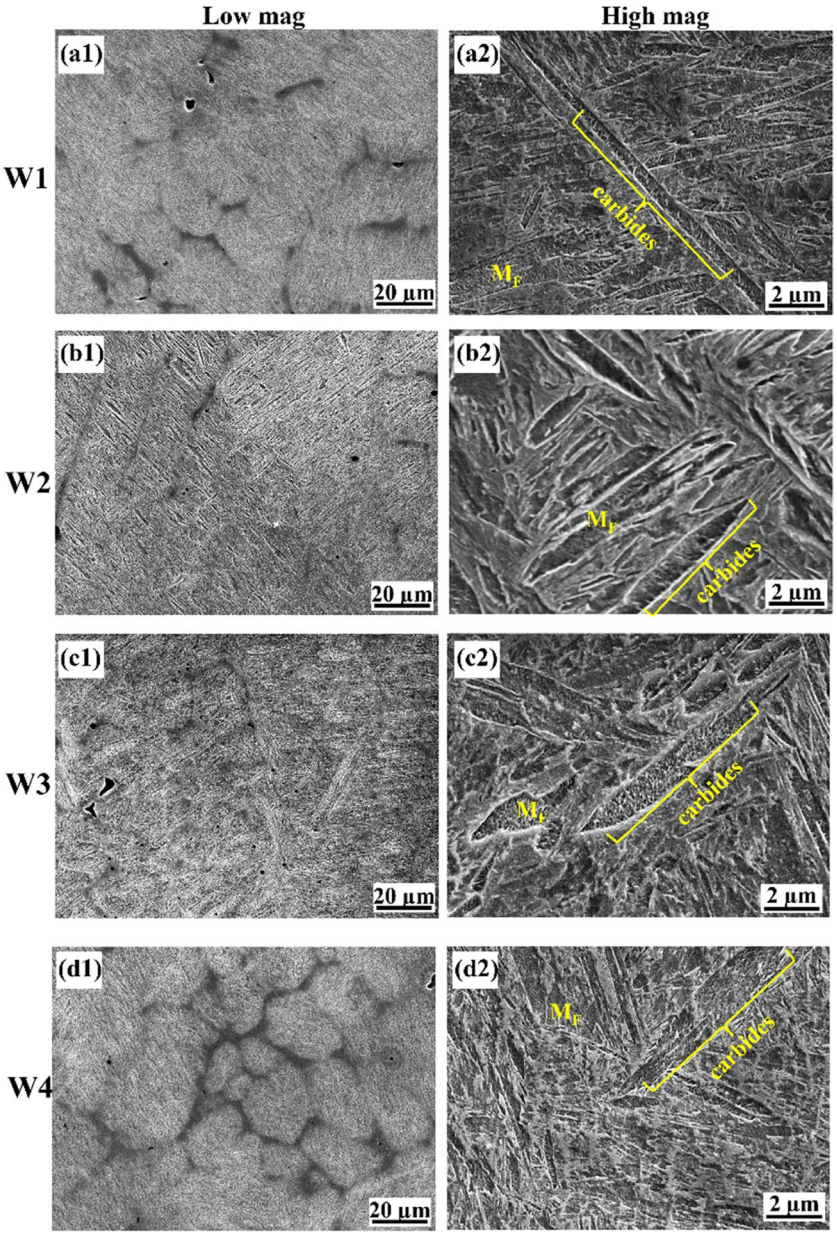

Fig. 7 SEM micrographs at different magnifications taken from the top region of walls deposited under different local shielding atmospheres: (a1, a2) W1; (b1, b2) W2; (c1, c2) W3; (d1, d2) W4

The thin light-etching curved bands present throughout the builds, as labelled Fig. 6, are consistent with being fusion boundaries, where the melting of solid was arrested during the deposition of each bead and solidification of the beads subsequently first began. They are comparatively fainter than the HAZ bands, as well as being narrower. The light-etching nature of these boundaries can be attributed to transient solute partitioning during the initial acceleration of the solidification front [31]. It is likely that these regions are depleted in solute, and hence form fewer carbides, therefore etching less darkly.

There was no reliably measurable systematic change in the HAZ band or fusion boundary features with changes in shielding gas composition.

3.3.4 Dendritic microsegregation

Figures 7, 8, and 9 show the presence of dendritic microsegregation patterns in all regions of all the builds. These features were investigated further by EDS analysis of build W1 (see Fig. 10). The interdendritic regions are shown to be enriched in Mo, Si, Mn, and Cr. Furthermore, some spherical particles (labelled by dashed circles) can be clearly observed within the enriched interdendritic regions, which are speculated to be MnS/Al_2O_3 inclusions. Enrichment of interdendritic regions in these elements and inclusions is expected and commonplace in low-alloy steels.

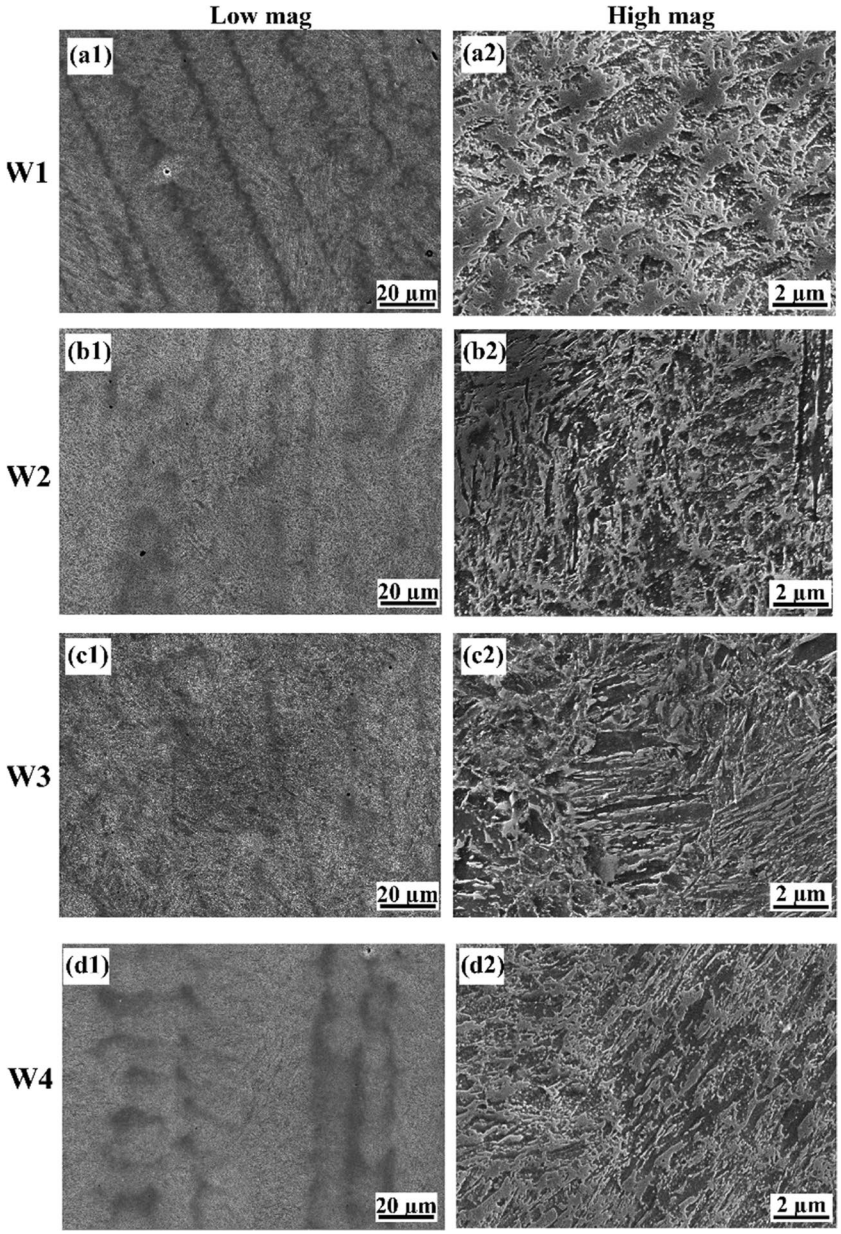

Fig. 8 SEM micrographs at different magnifications taken from the bulk regions of walls deposited under different local shielding atmospheres (images were taken between dark-etching HAZ bands): (a1, a2) W1; (b1, b2) W2; (c1, c2) W3; (d1, d2) W4

3.3.5 Grain morphology evolution

To better understand the evolution of the grain morphology (martensite and original austenite) during deposition, EBSD maps were taken from the cross-sectional plane of the W4 sample, as shown in Fig. 11. Figure 11(b1–2) shows the inverse pole figure (IPF) maps taken from the columnar and refined prior austenite zones, manifesting a comparatively fine lath-like martensitic microstructure in random crystallographic orientation throughout the sample. Such morphology is commonly observed in additively manufactured carbon steel [32] and martensitic stainless steel [33]. In each layer deposition and subsequent solidification, prior austenite grains (PAGs) grow towards the maximum heat flow direction from the solid–liquid interface [34]. When cooled down to martensite transformation temperature, a single PAG is transformed into crystallographic martensite variants satisfying Nishiyama–Wassermann (N-W) orientation relationship (OR) of $\{111\}_{\gamma}//\left\{1\bar{1}0\right\}_{\alpha'}\langle\bar{1}01\rangle_{\gamma}//\langle001\rangle_{\alpha'}$, leading to comparatively random texture in the as-deposited condition [35, 36]. The average martensite lath size in the top region was measured to be 10.2 µm, which was found to be coarser than that in the HAZ band and inter-band zones. It can be seen from Fig. 11(d) that the martensite lath size reduces away from the top and then undulates throughout the bulk of the build. This is in contrast to a conclusion obtained from a previous study [4] that multiple reheating

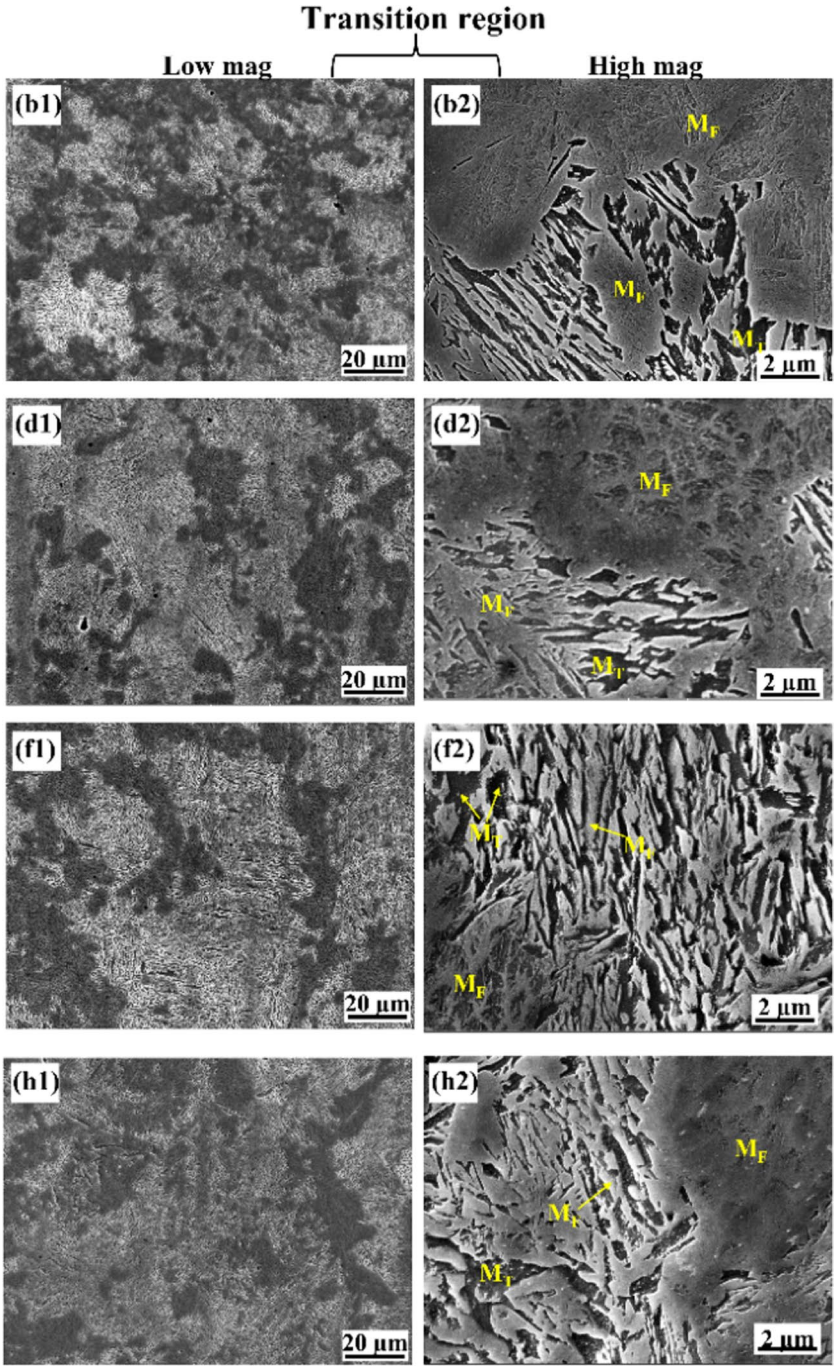

Fig. 9 SEM micrographs at different magnifications taken from the transition regions of walls deposited under different local shielding atmospheres: (a1, a2) W1; (b1, b2) W2; (c1, c2) W3; (d1, d2) W4

cycles in the middle region will lead to the growth of the martensitic grains—instead, it appears that the refinement of the PAG size that occurs from thermal cycling limits the size of the martensite moving away from the very top of the build.

The PAG structure in the cross-sectional plane of the W4 sample was reconstructed following the N-W OR (Fig. 11(c1, c2)). Coarse columnar PAGs with hundreds of microns and <100> directions parallel to the build direction predominate in the top half of the top region, while finer equiaxed grains only occurring in the bottom half of the top. In the bulk, both columnar and refined PAG morphologies can be seen, showing an alternating distribution. Throughout the build, the columnar PAGs will have been the products of direct epitaxial growth during solidification, while the equiaxed PAGs are likely to have been newly nucleated when the reheating temperature exceeded Ac_1 in subsequent passes—a certain range of the deposit below the fusion line is austenitized rapidly during the deposition process, forming new austenite grains. This also explains why

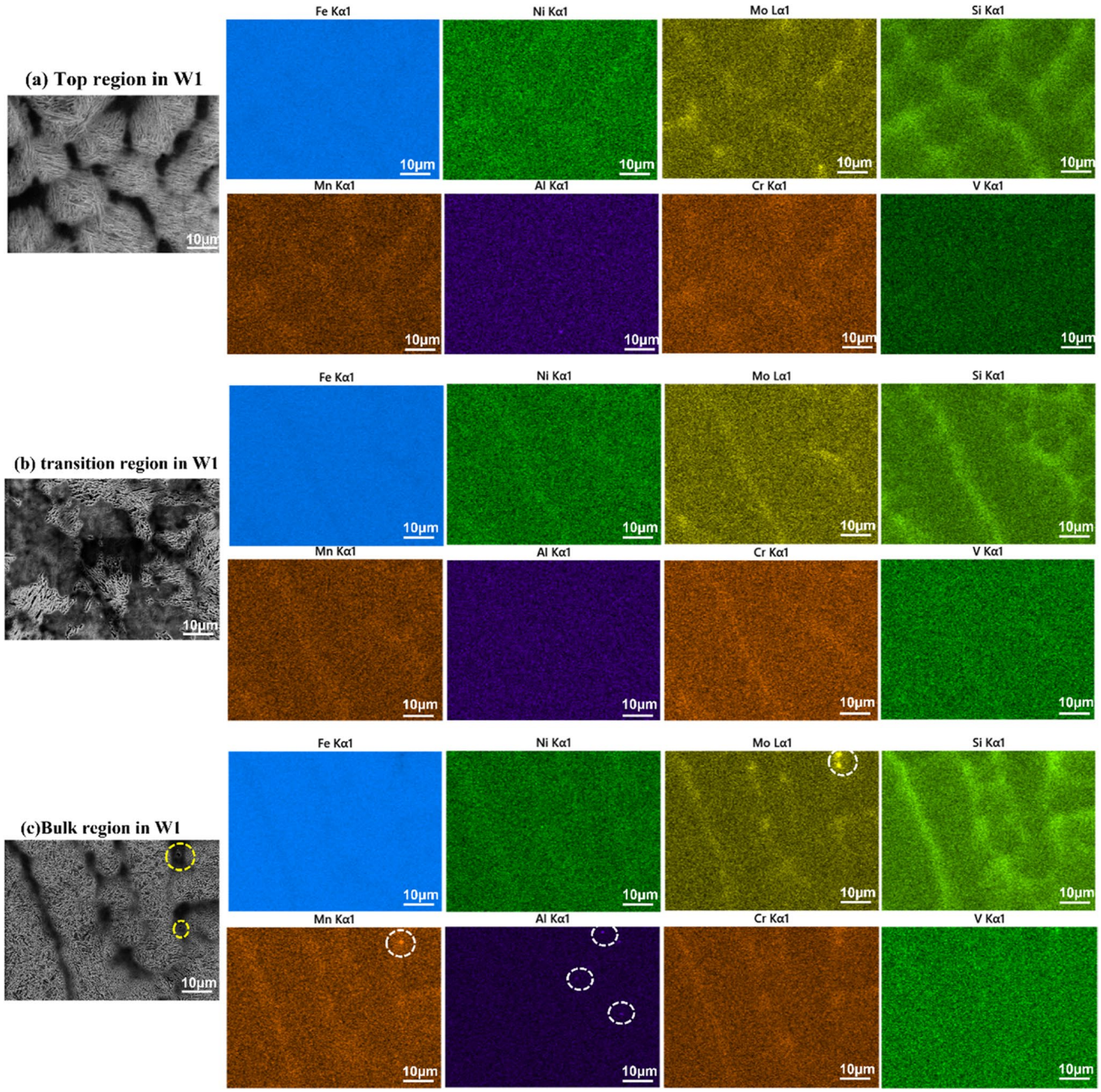

Fig. 10 SEM images and corresponding EDS maps of the W1 sample taken from different regions: **a** top region; **b** transition region, **c** bulk region

the columnar PGAs in the top region are generally coarser than those in the middle region.

3.4 Mechanical properties

The microhardness transitions from the top of the base plate to the top surface of the wall structures manufactured under different local shielding mixtures are presented in Fig. 12. It shows that the microhardness value fluctuated at around 450 HV in the bulk and then significantly increased to 620–650 HV when entering the top region. Such a hardness transition is consistent with the formation of tempered martensite and fresh untempered martensite in the bulk and top regions, respectively. During the in situ tempering process caused by the layer-by-layer thermal cycles, carbides would have gradually precipitated out from the martensitic matrix, leading to a decreasing supersaturation degree of carbon, and the dislocation density also would have likely decreased, leading

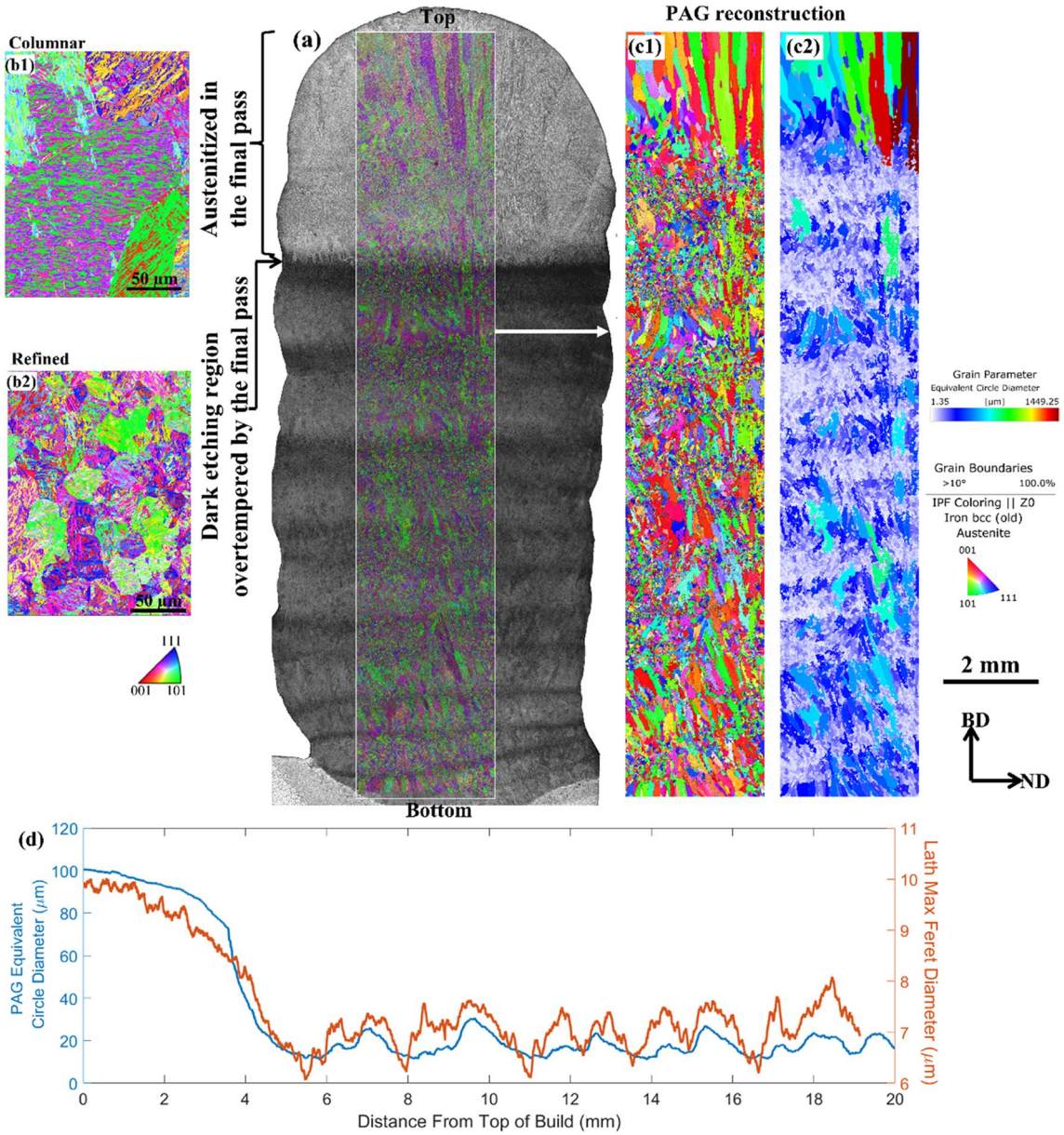

Fig. 11 (a) OM image taken from BD-ND plane of W4 sample showing the EBSD scanning area; IPF maps taken from the (b1) columnar prior austenite zone and (b2) refined prior austenite region; (c1) reconstructed prior austenite orientation map, (c2) corresponding reconstructed austenite grain (PAG) size distribution map, (d) variation of reconstructed PAG equivalent circle diameter (ECD) and martensitic lath max ferret diameter with the distance from the top of the build

to low hardness levels [37]. It might have been expected that the average microhardness values both in the bulk and top regions would decrease gradually with the increased CO_2 content in the local shielding atmosphere, since more heat would have been generated when introducing more CO_2 into the local shielding mixture, leading to a greater tempering effect and slower cooling rates. However, no trend could be distinguished above the scatter in results. Similarly, no statistically significant change in hardness was detected when replacing 38% of Ar with He.

Due to the location dependence of microhardness values, three tensile coupons were extracted from both the top and bulk regions of the wall structures under different shielding gas mixtures to further examine the tensile performances. The room-temperature tensile stress–strain curves and corresponding properties of the specimens are shown in Fig. 13. It can be seen that the strength in the top region is higher than that in the bulk region, while the ductility showed the contrary trend regardless of the shielding gas mixture conditions. Necking can be clearly observed on the fractured

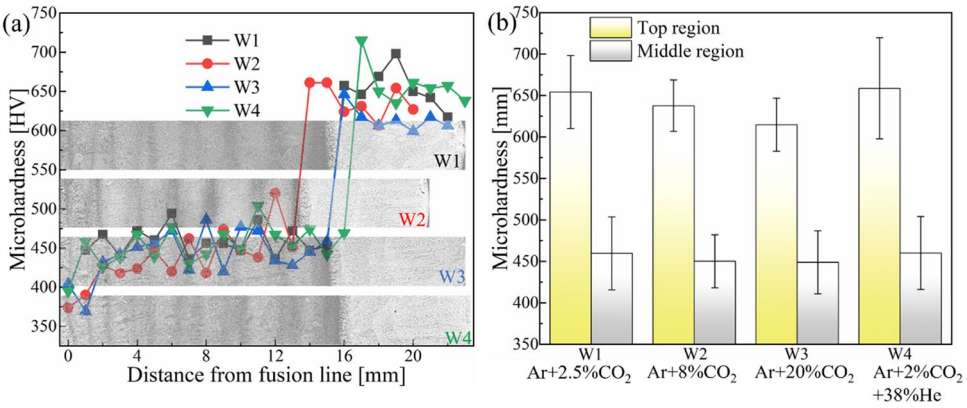

Fig. 12 **a** Microhardness transition and **b** corresponding average microhardness values of the single-pass wall components manufactured under various local shielding gas mixtures

tensile specimens extracted from bulk regions (Fig. 13b) and is not so evident in the top region specimens, reflecting better plasticity in the bulk of the walls. There are several strengthening mechanisms in polycrystalline alloys, including solid solution, precipitation, dislocation, and grain boundary strengthening. Due to the multiple thermal cycles in the deposition process, which can be viewed as an in situ tempering treatment, carbide precipitates (e.g., cementite) are formed, which contribute to strengthening. Nevertheless, it is well known that their strengthening effect is outweighed by the loss of carbon presence in solution or pinning dislocations and also by the loss of dislocation density during the tempering thermal cycles (this is why tempering martensite decreases its strength in general). Since the average grain size of the top region (whether martensite or original austenite) is coarser than the bulk part, the effect of grain boundary strengthening here is clearly offset by martensite strengthening. In comparison, the shielding gas mixtures from the torch exert a much lesser influence on strength and ductility compared with deposition location—no trends can be confidently discerned with respect to shielding gas mixture.

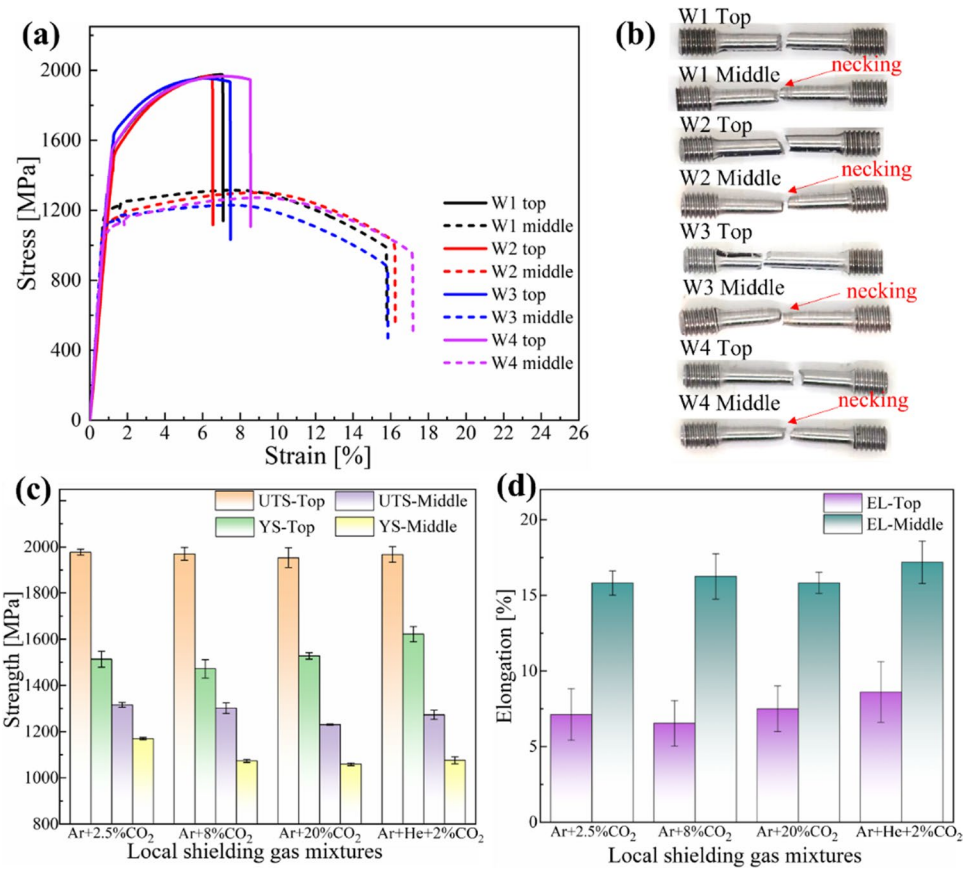

Fig. 13 **a** Room-temperature tensile stress–strain curves, **b** fractured tensile specimens, **c** corresponding strength including ultimate tensile strength (UTS) and yield strength (YS), and **d** elongation (EL) at fracture in the top and middle regions of single-pass walls manufactured under different local shielding atmospheres

The fracture morphologies in different regions of the wall components deposited under different local shielding gas mixtures are shown in Fig. 14. Distinct differences in fracture morphologies can be found between the top and bulk regions. The fracture cross-section in the top region samples is larger than in the bulk samples, which is consistent with the reduction of area and ductility in the top region being smaller than that in the middle. By magnifying, it can be found that the fracture morphology in the top region consists of quasi-cleavage facets, tearing ridges and shallow dimples, indicating a mixed mode of ductile and brittle fracture. The development of quasi-cleavage facets could be attributed to the difficulty inhibiting crack initiation and propagation by untempered martensite at the top region [4]. In comparison, the fractured bulk region specimens mainly consist of deep dimples with cementite particles inside and some fine-facet cracks, indicating a mixed fracture but more inclined to ductile fracture. These cracks are formed where cleavage occurs, indicating that a cleavage-detaching mechanism may have been associated with the boundaries of the martensite blocks [38]. Therefore, it can be seen that the ductile characteristics in tensile fracture morphology increase from the top region to the reheated bulk region, which is in accordance with the elongation data. Besides, the effects of local shielding gas mixtures on the fracture morphology appear to be negligible compared to the deposition location. Nevertheless, the largest concentration of dimples was measured in the bulk of W4 and the smallest concentration in the bulk of W3 in Fig. 14b, d, f, and h, consistent with the highest and poorest elongation being achieved in W4 and W3, respectively.

Table 4 summarizes the tensile properties of 300 M UHSS produced by various AM processes in previous studies. The bulk region of GMA-WAAM 300 M UHSS possesses comparatively lower strength but higher ductility than the CMT-WAAM products, which could be attributed to a higher thermal input increasing the level of tempering.

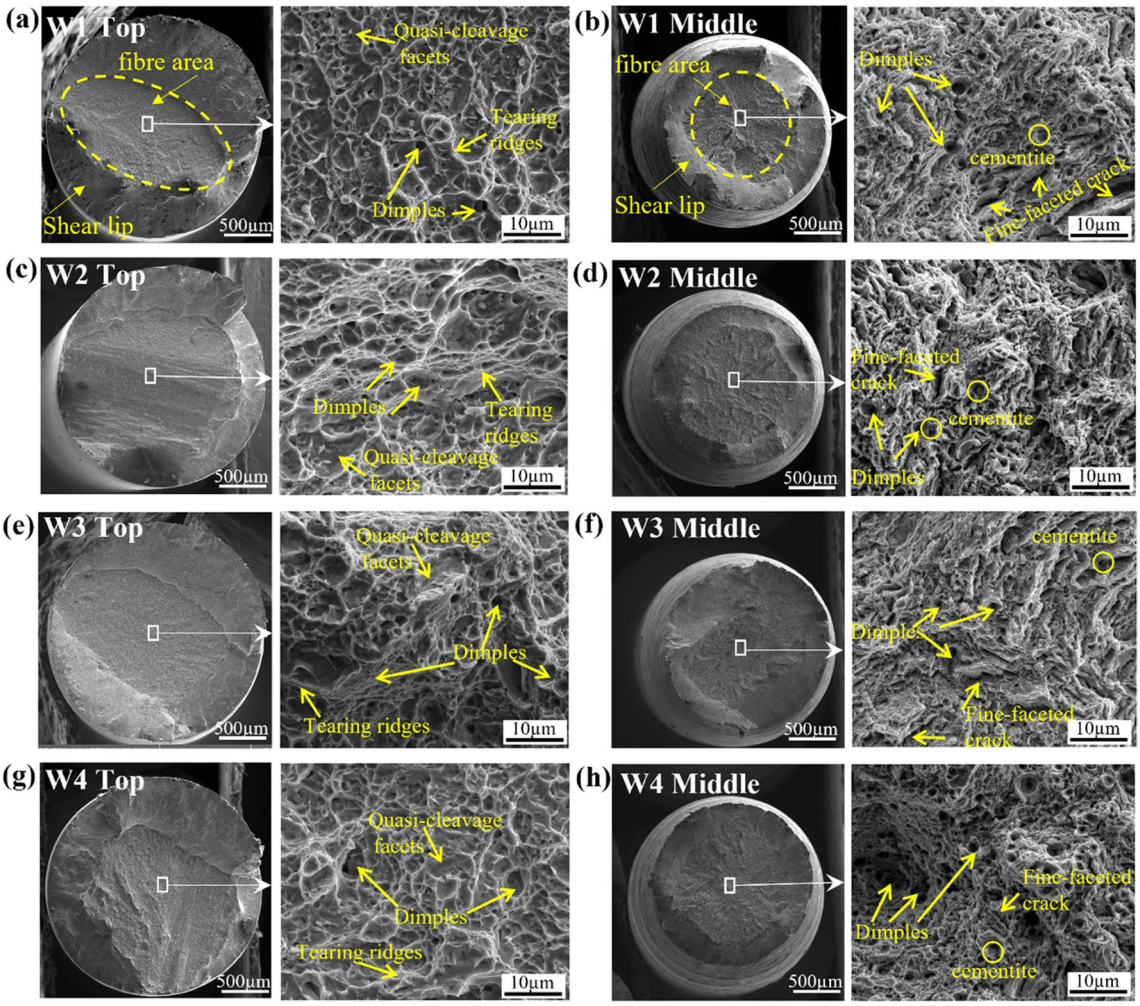

Fig. 14 Tensile fracture morphologies in different regions of the walls deposited under different local shielding gas mixtures: **a** top and **b** middle regions of W1; **c** top and **d** middle regions of W2; **e** top and **f** middle regions of W3; **g** top and **h** middle regions of W4

However, GMA 300 M bulk possesses similar strength as the laser-powder-based AM product in the as-deposit condition, but the elongation is much higher, which could be attributed to different energy density, porosity level (this tends to be higher in powder-based AM), and tensile coupon design. Compared with the AMS6419K standard of 300 M UHSS forgings, the top region of GMA 300 M studied here possesses comparable strength but comparatively lower ductility. While the ductility of the GMA 300 M bulk region is much higher than the forged one, the strength is far away from the lower limit of the standard. These observations are consistent with the top region being under-tempered, and the bulk region being over-tempered in the as-built state. Therefore, it is clear that in the as-deposit condition, the tensile properties of all AM 300 M UHSS do not meet the standard and need to be heat treated. Therefore, in future research, comprehensive post-heat treatment investigations will be carried out to make the final mechanical properties meet the standard.

4 Conclusions

In this investigation, 300 M ultra-high-strength steel single-pass components were deposited by wire-based gas metal arc additive manufacturing. The influences of torch shielding gas mixture composition on the process stability, morphology, microstructure, and mechanical performance were systematically studied. The main findings are summarized below:

1. With the increase of CO_2 addition in the torch shielding gas, the arc length decreased so that the transfer mode changed from spray mode to droplet mode. In addition, replacing 38% of Ar with He led to a broader arc core, a slightly shorter arc length and maintained a spray transfer.
2. The 300 M wall surface roughness became coarser with the increasing CO_2 proportion due to severer spatter, leading to worse surface quality. A comparatively better wall surface quality was found when replacing 38% of Ar with He in combination with ~2% CO_2.
3. Adding CO_2 and He in pure Ar significantly increased the bead width and penetration. The more the addition of CO_2, the broader the bead width and HAZ width became. Furthermore, a decreasing trend in wall height was found when CO_2 content in the shielding gas mixture increased from 2.5 to 8%. In addition, the bead and wall dimensions kept similar when replacing Ar with He.
4. The microstructure differed between the top and the bulk of all the 300 M wall structures: fresh as-quenched martensite with auto-tempered carbides and mainly coarse columnar PAGs inside the top region, and over-tempered martensite with a variable PAG morphology in the bulk. Generally, shielding gas composition did not have a measurable effect on the microstructural evolution observed.
5. The microhardness and tensile properties show a distinct location dependence in all shielding gas conditions. The microhardness and strength in the top region were higher than that in the bulk region, while the plasticity showed a contrary trend. The torch-shielding gas mixtures did not appear to influence strength and ductility and hence had a much less significant effect than deposition location.
6. Compared with the AMS6417K standard of 300 M UHSS forgings, the as-built GMA 300 M does not meet the standard and must be heat treated. Therefore, for the next step, comprehensive post-heat treatment research will be carried out with the purpose of making the final mechanical properties meet the standard.

This study provides a reference for the subsequent application of metal inert gas arc additive manufacturing

Table 4 Comparison of tensile properties of 300 M manufactured by various AM processes (on average)

Techniques	Condition	UTS [MPa]	YS [MPa]	EL[%]
GMA-WAAM	AD [this study]	Top: 1967 Bulk: 1280	1534 1095	7.4 16.3
CMT-WAAM	AD [4]	1508	932	13.4
	HT(970°C/1 h/OQ + 300°C/2 h/AC/twice) [39]	1942	1707	12.6
GTA-WAAM	AD [40]	1540	-	6.7
PBF-SLM	AD [1]	1156–1193	1085–1145	6.8–9.1
LDED	AD [7]	1400–1500	979–1170	7.7–11.5
	HT(870 °C/1 h/OQ + 310 °C/2 h/AC/twice) [41]	1966	1661	8–9
AMS6419K standard		≥ 1931	≥ 1586	≥ 7

to aircraft landing gear mass production to achieve a high deposition rate and ensure process stability simultaneously.

Acknowledgements The authors would also like to acknowledge the raw material support from Airbus. The authors would also like to acknowledge facilities access and support from the Henry Royce Institute through EPSRC grants EP/R00661X/1, EP/S019367/1, EP/P025021/1, and EP/P025498/1. The authors would also like to thank the technical support from Nisar Shah and Steve Pope.

Author contribution JW: conceptualization, methodology, investigation, data analysis, and writing—original draft.

CD: investigation, data analysis, and writing (review and editing).

MT: investigation, data analysis, and writing (review and editing).

CW: investigation, data analysis, and writing (review and editing).

EP: investigation, data analysis, writing (review and editing), and project administration.

JD: investigation, resources, supervision, and project administration.

MP: investigation, resources, and project administration.

SW: investigation, resources, writing (review and editing), supervision, and project administration.

All authors read and approved the final manuscript.

Funding This work is financially supported by the "Hybrid Direct Energy Deposition Sprint" project (NO.113345_ATI Sprint Hybrid DED) funded by the Aerospace Technology Institute (ATI).

Declarations

Conflict of interest The authors declare no competing interests.

References

1. Jing G, Huang W, Gao P, Meng L, Yang H, Wang Z (2020) Formability, microstructure and mechanical properties of 300M steel single tracks fabricated by high power selective laser melting. Opt Laser Technol 131. https://doi.org/10.1016/j.optlastec.2020.106434.
2. He X, Yang X, Zhang G, Li J, Hu H (2012) Quenching microstructure and properties of 300M ultra-high strength steel electron beam welded joints. Mater Des 40:386–391. https://doi.org/10.1016/j.matdes.2012.04.010
3. Jing G, Z Wang (2021) Defects, densification mechanism and mechanical properties of 300M steel deposited by high power selective laser melting. Addit Manuf 38. https://doi.org/10.1016/j.addma.2020.101831
4. Xiong YB, Wen DX, Zheng ZZ, Li JJ (2022) Effect of interlayer temperature on microstructure evolution and mechanical performance of wire arc additive manufactured 300M steel. Mater Sci Eng A 831. https://doi.org/10.1016/j.msea.2021.142351.
5. Wang J, Pan Z, Wei L, He S, Cuiuri D, Li H (2019) Introduction of ternary alloying element in wire arc additive manufacturing of titanium aluminide intermetallic. Addit Manuf 27:236–245. https://doi.org/10.1016/j.addma.2019.03.014
6. Dirisu P, Ganguly S, Mehmanparast A, Martina F, Williams S (2019) Analysis of fracture toughness properties of wire + arc additive manufactured high strength low alloy structural steel components. Mater Sci Eng A 765. https://doi.org/10.1016/j.msea.2019.138285.
7. Liu F et al (2015) Microstructure and mechanical properties of laser solid formed 300M steel. J Alloys Compd 621:35–41. https://doi.org/10.1016/j.jallcom.2014.09.111
8. Barr C, Da Sun S, Easton M, Orchowski N, Matthews N, Brandt M (2020) Influence of delay strategies and residual heat on in-situ tempering in the laser metal deposition of 300M high strength steel. Surf Coat Technol 383. https://doi.org/10.1016/j.surfcoat.2019.125279.
9. Jing G, Huang W, Yang H, Wang Z (2020) Microstructural evolution and mechanical properties of 300M steel produced by low and high power selective laser melting. J Mater Sci Technol 48:44–56. https://doi.org/10.1016/j.jmst.2019.12.020
10. Jing G, Wang Z (2021) Influence of molten pool mode on microstructure and mechanical properties of heterogeneously tempered 300M steel by selective laser melting. J Mater Process Technol 296. https://doi.org/10.1016/j.jmatprotec.2021.117188
11. Wang J et al (2018) Characterization of wire arc additively manufactured titanium aluminide functionally graded material: microstructure, mechanical properties and oxidation behaviour. Mater Sci Eng A 734:110–119. https://doi.org/10.1016/j.msea.2018.07.097
12. Wang C, Suder W, Ding J, Williams S (2021) Wire based plasma arc and laser hybrid additive manufacture of Ti-6Al-4V. J Mater Process Technol 293. https://doi.org/10.1016/j.jmatprotec.2021.117080
13. Marques DA, Oliveira JP, Baptista AC (2023) A short review on the corrosion behaviour of wire and arc additive manufactured materials. Metals 13(641):1–19. https://doi.org/10.3390/met13040641
14. Felice IO, Shen JJ, Barragan AFC et al (2023) Wire and arc additive manufacturing of Fe-based shape memory alloys: Microstructure, mechanical and functional behavior. Mater Des 231:112004. https://doi.org/10.1016/j.matdes.2023.112004
15. Wang LW, Wu T, Wang DL et al (2023) A novel heterogeneous multi-wire indirect arc directed energy deposition for in-situ synthesis Al-Zn-Mg-Cu alloy: process, microstructure and mechanical properties. 2:103639, https://doi.org/10.1016/j.addma.2023.103639
16 Cam G (2022) Prospects of producing aluminum parts by wire arc additive manufacturing (WAAM). Mater Today: Proceed 62(part 1):77–85. https://doi.org/10.1016/j.matpr.2022.02.137
17. Bolukbasi OS, Serindag T, Gurol U, Gunen A, Cam G (2023) Improving oxidation resistance of wire arc additive manufactured Inconel 625 Ni-based superalloy by pack aluminizing. CIRP J Manuf Sci Tech 46:89–97. https://doi.org/10.1016/j.cirpj.2023.07.011
18. Gurol U, Altinay Y, Gunen A, Bolukbasi OS, Kocak M, Cam G (2023) Effect of powder-pack aluminizing on microstructure and oxidation resistance of wire arc additively manufactured stainless steels. Surf Coat Technol 468:129742. https://doi.org/10.1016/j.surfcoat.2023.129742
19. Gunen A, Gurol U, Kocak M, Cam G (2023) A new approach to improve some properties of wire arc additively manufactured stainless steel components: simultaneous homogenization and

boriding. Surf Coat Technol 460:129395. https://doi.org/10.1016/j.surfcoat.2023.129395
20. Gunen A, Gurol U, Kocak M, Cam G (2023) Investigation into the influence of boronizing on the wear behavior of additively manufactured Inconel 625 alloy at elevated temperature. Prog in Addi Manuf. https://doi.org/10.1007/s40964-023-00398-8
21. Kim JD, Kim JW, Cheon JY, Do Kim Y, Ji C (2020) Effect of shielding gases on the wire arc additive manufacturability of 5 Cr – 4 Mo tool steel for die casting mold making. J Korean Ins Metals Mater 58(12):852–862. https://doi.org/10.3365/KJMM.2020.58.12.852
22. Kah P, Martikainen J (2013) Influence of shielding gases in the welding of metals. Inter J Adv Manuf Technol 64(9–12):1411–1421. https://doi.org/10.1007/s00170-012-4111-6
23. Mvola B, Kah P (2017) Effects of shielding gas control: welded joint properties in GMAW process optimization. Inter J Adv Manuf Technol vol. 88, no. 9–12. Springer London, pp. 2369–2387. https://doi.org/10.1007/s00170-016-8936-2
24. Wang LL, Lu FG, Wang HP, Murphy AB, Tang XH (2014) Effects of shielding gas composition on arc profile and molten pool dynamics in gas metal arc welding of steels. J Phys D Appl Phys 47(46). https://doi.org/10.1088/0022-3727/47/46/465202
25. Chen R, Zheng Z, Li N, Li J, Feng F (2018) In-situ investigation of phase transformation behaviors of 300M steel in continuous cooling process. Mater Charact 144:400–410. https://doi.org/10.1016/j.matchar.2018.07.034
26. Wang J et al (2020) Evolution of crystallographic orientation, precipitation, phase transformation and mechanical properties realized by enhancing deposition current for dual-wire arc additive manufactured Ni-rich NiTi alloy. Addit Manuf 34. https://doi.org/10.1016/j.addma.2020.101240
27. Hidalgo J, Celada-Casero C, Santofimia MJ (2019) Fracture mechanisms and microstructure in a medium Mn quenching and partitioning steel exhibiting macrosegregation. Mater Sci Eng A 754:766–777. https://doi.org/10.1016/j.msea.2019.03.055
28. Wang XL, Wang XM, Shang CJ, Misra RDK (2015) Characterization of the multi-pass weld metal and the impact of retained austenite obtained through intercritical heat treatment on low temperature toughness. Mater Sci Eng A 649:282–292. https://doi.org/10.1016/j.msea.2015.09.030
29. Li Y, Wu S, Li H, Dong Y, Cheng F (2021) Submerged arc additive manufacturing (SAAM) of low-carbon steel: Effect of in-situ intrinsic heat treatment (IHT) on microstructure and mechanical properties. Addit Manuf 46. https://doi.org/10.1016/j.addma.2021.102124
30 Davis AE, Caballero AE, Biswal R, Williams S, Prangnell PB (2022) Comparison of microstructure refinement in wire-arc additively manufactured Ti–6Al–2Sn–4Zr–2Mo–0.1Si and Ti–6Al–4V built with inter-pass deformation. Metall Mater Trans A Phys Metall Mater Sci. https://doi.org/10.1007/s11661-022-06811-1
31. Ho A, Zhao H, Fellowes JW, Martina F, Davis AE, Prangnell PB (2019) On the origin of microstructural banding in Ti-6Al4V wire-arc based high deposition rate additive manufacturing. Acta Mater 166:306–323. https://doi.org/10.1016/j.actamat.2018.12.038
32. Gui Y, Bian H, Aoyagi K, Chiba A (2022) Microstructure evolution and hardness of S30C carbon steel produced by powder bed fusion using an electron beam and subsequent heat treatments. Mater Lett 328. https://doi.org/10.1016/j.matlet.2022.133096
33. Salahi S, Nemani AV, Ghaffari M, Lunde J, Nasiri A, (2021) On microstructure, crystallographic orientation, and corrosion properties of wire arc additive manufactured 420 martensitic stainless steel: Effect of the inter-layer temperature. Addit Manuf 46. https://doi.org/10.1016/j.addma.2021.102157
34. Lek YZ, Wang C, Shen X, Chen Z, Ramamurty U, Zhou K (2022) Additive manufacturing of corrosion-resistant maraging steel M789 by directed energy deposition. Mater Sci Eng A 857. https://doi.org/10.1016/j.msea.2022.144032
35. Bajaj P, Hariharan A, Kini A, Kürnsteiner P, Raabe D, Jägle EA (2020) Steels in additive manufacturing: a review of their microstructure and properties. Mater Sci Eng A 772. https://doi.org/10.1016/j.msea.2019.138633
36. Lu Y et al (2020) Influence of hot compressive parameters on flow behaviour and microstructure evolution in a commercial medium carbon micro-alloyed spring steel. J Manuf Process 58:1171–1181. https://doi.org/10.1016/j.jmapro.2020.09.021
37. Tanvir ANM et al (2021) Phase stability and mechanical properties of wire + arc additively manufactured H13 tool steel at elevated temperatures. J Mater Sci Technol 67:80–94. https://doi.org/10.1016/j.jmst.2020.04.085
38. Pandey C, Saini N, Mahapatra MM, Kumar P (2017) Study of the fracture surface morphology of impact and tensile tested cast and forged (C&F) Grade 91 steel at room temperature for different heat treatment regimes. Eng Fail Anal 71:131–147. https://doi.org/10.1016/j.engfailanal.2016.06.012
39. Xiong YB, Wen DX, Zheng ZZ, Sun CY, Xie J, Li JJ (2023) Effect of heat treatment on microstructure and mechanical properties of directed energy deposition-Arc 300M steel. Mater Charact 198:112756. https://doi.org/10.1016/j.matchar.2023.112756
40. Skiba T, Baufeld B, Van Der Biest O (2011) Shaped metal deposition of 300M steel. Proc Inst Mech Eng B J Eng Manuf 225(6):831–839. https://doi.org/10.1177/09544054JEM2115
41. Liu F et al (2016) Effect of tempering temperature on microstructure and mechanical properties of laser solid formed 300M steel. J Alloys Compd 689:225–232. https://doi.org/10.1016/j.jallcom.2016.07.276

2023-11-01

Investigation of 300M ultra-high-strength steel deposited by wire-based gas metal arc additive manufacturing

Wang, Jun

Springer

Wang J, Diao C, Taylor M, et al., (2023) Investigation of 300M ultra-high-strength steel deposited by wire-based gas metal arc additive manufacturing. The International Journal of Advanced Manufacturing Technology, Available online 1 November 2023

https://doi.org/10.1007/s00170-023-12566-9